



Fig. 3. Theory, presented as the experiment (see Fig. 1). The SHG source is the magnetic component of the Lorentz force on metal electrons in the SRRs.

The setup for measuring the SHG is described in the supporting online material (22). We expect that the SHG strongly depends on the resonance that is excited. Obviously, the incident polarization and the detuning of the laser wavelength from the resonance are of particular interest. One possibility for controlling the detuning is to change the laser wavelength for a given sample, which is difficult because of the extremely broad tuning range required. Thus, we follow an alternative route, lithographic tuning (in which the incident laser wavelength of 1.5 μm , as well as the detection system, remains fixed), and tune the resonance positions by changing the SRR size. In this manner, we can also guarantee that the optical properties of the SRR constituent materials are identical for all configurations. The blue bars in Fig. 1 summarize the measured SHG signals. For excitation of the LC resonance in Fig. 1A (horizontal incident polarization), we find an SHG signal that is 500 times above the noise level. As expected for SHG, this signal closely scales with the square of the incident power (Fig. 2A). The polarization of the SHG emission is nearly vertical (Fig. 2B). The small angle with respect to the vertical is due to deviations from perfect mirror symmetry of the SRRs (see electron micrographs in Fig. 1). Small detuning of the LC resonance toward smaller wavelength (i.e., to 1.3- μm wavelength) reduces the SHG signal strength from 100% to 20%. For excitation of the Mie resonance with vertical incident polarization in Fig. 1D, we find a small signal just above the noise level. For excitation of the Mie resonance with horizontal incident polarization in Fig. 1C, a small but significant SHG emission is found, which is again po-

larized nearly vertically. For completeness, Fig. 1B shows the off-resonant case for the smaller SRRs for vertical incident polarization.

Although these results are compatible with the known selection rules of surface SHG from usual nonlinear optics (23), these selection rules do not explain the mechanism of SHG. Following our above argumentation on the magnetic component of the Lorentz force, we numerically calculate first the linear electric and magnetic field distributions (22); from these fields, we compute the electron velocities and the Lorentz-force field (fig. S1). In the spirit of a metamaterial, the transverse component of the Lorentz-force field can be spatially averaged over the volume of the unit cell of size a by t . This procedure delivers the driving force for the transverse SHG polarization. As usual, the SHG intensity is proportional to the square modulus of the nonlinear electron displacement. Thus, the SHG strength is expected to be proportional to the square modulus of the driving force, and the SHG polarization is directed along the driving-force vector. Corresponding results are summarized in Fig. 3 in the same arrangement as Fig. 1 to allow for a direct comparison between experiment and theory. The agreement is generally good, both for linear optics and for SHG. In particular, we find a much larger SHG signal for excitation of those two resonances (Fig. 3, A and C), which are related to a finite magnetic-dipole moment (perpendicular to the SRR plane) as compared with the purely electric Mie resonance (Figs. 1D and 3D), despite the fact that its oscillator strength in the linear spectrum is comparable. The SHG polarization in the theory is strictly vertical for all resonances. Quantitative deviations between the SHG signal strengths of experiment and theory, respectively, are probably due to the simplified SRR shape assumed in our calculations and/or due to the simplicity of our modeling. A systematic microscopic theory of the nonlinear optical properties of metallic

metamaterials would be highly desirable but is currently not available.

References and Notes

1. J. B. Pendry, A. J. Holden, D. J. Robbins, W. J. Stewart, *IEEE Trans. Microw. Theory Tech.* **47**, 2075 (1999).
2. J. B. Pendry, *Phys. Rev. Lett.* **85**, 3966 (2000).
3. R. A. Shelby, D. R. Smith, S. Schultz, *Science* **292**, 77 (2001).
4. T. J. Yen *et al.*, *Science* **303**, 1494 (2004).
5. S. Linden *et al.*, *Science* **306**, 1351 (2004).
6. C. Enkrich *et al.*, *Phys. Rev. Lett.* **95**, 203901 (2005).
7. A. N. Grigorenko *et al.*, *Nature* **438**, 335 (2005).
8. G. Dolling, M. Wegener, S. Linden, C. Hormann, *Opt. Express* **14**, 1842 (2006).
9. G. Dolling, C. Enkrich, M. Wegener, C. M. Soukoulis, S. Linden, *Science* **312**, 892 (2006).
10. J. B. Pendry, D. Schurig, D. R. Smith, *Science* **312**, 1780; published online 25 May 2006.
11. U. Leonhardt, *Science* **312**, 1777 (2006); published online 25 May 2006.
12. M. W. Klein, C. Enkrich, M. Wegener, C. M. Soukoulis, S. Linden, *Opt. Lett.* **31**, 1259 (2006).
13. W. J. Padilla, A. J. Taylor, C. Highstreet, M. Lee, R. D. Averitt, *Phys. Rev. Lett.* **96**, 107401 (2006).
14. D. R. Smith, S. Schultz, P. Markos, C. M. Soukoulis, *Phys. Rev. B* **65**, 195104 (2002).
15. S. O'Brien, D. McPeake, S. A. Ramakrishna, J. B. Pendry, *Phys. Rev. B* **69**, 241101 (2004).
16. J. Zhou *et al.*, *Phys. Rev. Lett.* **95**, 223902 (2005).
17. A. K. Popov, V. M. Shalaev, available at <http://arxiv.org/abs/physics/0601055> (2006).
18. V. G. Veselago, *Sov. Phys. Usp.* **10**, 509 (1968).
19. M. Wegener, *Extreme Nonlinear Optics* (Springer, Berlin, 2004).
20. H. M. Barlow, *Nature* **173**, 41 (1954).
21. S.-Y. Chen, M. Maksimchuk, D. Umstadter, *Nature* **396**, 653 (1998).
22. Materials and Methods are available as supporting material on Science Online.
23. P. Guyot-Sionnest, W. Chen, Y. R. Shen, *Phys. Rev. B* **33**, 8254 (1986).
24. We thank the groups of S. W. Koch, J. V. Moloney, and C. M. Soukoulis for discussions. The research of M.W. is supported by the Leibniz award 2000 of the Deutsche Forschungsgemeinschaft (DFG), that of S.L. through a Helmholtz-Hochschul-Nachwuchsgruppe (VH-NG-232).

Supporting Online Material

www.sciencemag.org/cgi/content/full/313/5786/502/DC1
Materials and Methods
Figs. S1 and S2
References

26 April 2006; accepted 22 June 2006
10.1126/science.1129198

Reducing the Dimensionality of Data with Neural Networks

G. E. Hinton* and R. R. Salakhutdinov

High-dimensional data can be converted to low-dimensional codes by training a multilayer neural network with a small central layer to reconstruct high-dimensional input vectors. Gradient descent can be used for fine-tuning the weights in such "autoencoder" networks, but this works well only if the initial weights are close to a good solution. We describe an effective way of initializing the weights that allows deep autoencoder networks to learn low-dimensional codes that work much better than principal components analysis as a tool to reduce the dimensionality of data.

Dimensionality reduction facilitates the classification, visualization, communication, and storage of high-dimensional data. A simple and widely used method is principal components analysis (PCA), which

finds the directions of greatest variance in the data set and represents each data point by its coordinates along each of these directions. We describe a nonlinear generalization of PCA that uses an adaptive, multilayer "encoder" network

to transform the high-dimensional data into a low-dimensional code and a similar “decoder” network to recover the data from the code.

Department of Computer Science, University of Toronto, 6 King's College Road, Toronto, Ontario M5S 3G4, Canada.

*To whom correspondence should be addressed; E-mail: hinton@cs.toronto.edu

Starting with random weights in the two networks, they can be trained together by minimizing the discrepancy between the original data and its reconstruction. The required gradients are easily obtained by using the chain rule to backpropagate error derivatives first through the decoder network and then through the encoder network (1). The whole system is

called an “autoencoder” and is depicted in Fig. 1.

It is difficult to optimize the weights in nonlinear autoencoders that have multiple hidden layers (2–4). With large initial weights, autoencoders typically find poor local minima; with small initial weights, the gradients in the early layers are tiny, making it infeasible to train autoencoders with many hidden layers. **If the initial weights are close to a good solution, gradient descent works well**, but finding such initial weights requires a very different type of algorithm that learns one layer of features at a time. We introduce this “pretraining” procedure for binary data, generalize it to real-valued data, and show that it works well for a variety of data sets.

An ensemble of binary vectors (e.g., images) can be modeled using a two-layer network called a “restricted Boltzmann machine” (RBM) (5, 6) in which stochastic, binary pixels are connected to stochastic, binary feature detectors using symmetrically weighted connections. The pixels correspond to “visible” units of the RBM because their states are observed; the feature detectors correspond to “hidden” units. A joint **configuration (v, h)** of the visible and hidden units has an energy (7) given by

$$E(\mathbf{v}, \mathbf{h}) = - \sum_{i \in \text{pixels}} b_i v_i - \sum_{j \in \text{features}} b_j h_j - \sum_{i,j} v_i h_j w_{ij} \quad (1)$$

where v_i and h_j are the binary states of pixel i and feature j , b_i and b_j are their biases, and w_{ij} is the weight between them. The network assigns a probability to every possible image via this energy function, as explained in (8). The probability of a training image can be raised by

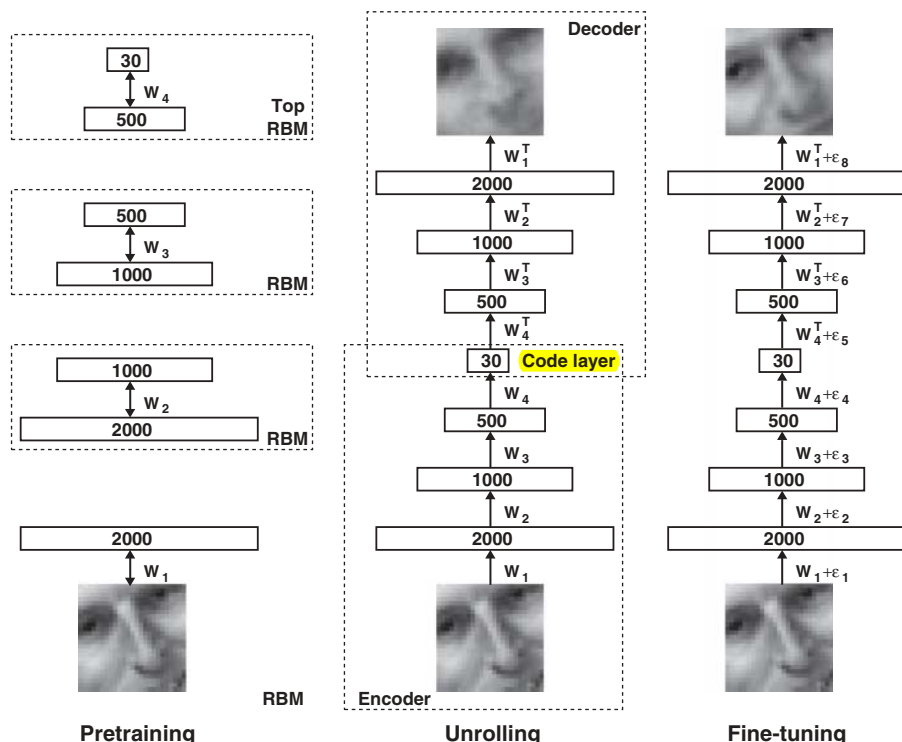


Fig. 1. Pretraining consists of learning a stack of restricted Boltzmann machines (RBMs), each having only one layer of feature detectors. The learned feature activations of one RBM are used as the “data” for training the next RBM in the stack. After the pretraining, the RBMs are “unrolled” to create a deep autoencoder, which is then fine-tuned using backpropagation of error derivatives.

Fig. 2. (A) Top to bottom: Random samples of curves from the test data set; reconstructions produced by the six-dimensional deep autoencoder; reconstructions by “logistic PCA” (8) using six components; reconstructions by logistic PCA and standard PCA using 18 components. The average squared error per image for the last four rows is 1.44, 7.64, 2.45, 5.90. (B) Top to bottom: A random test image from each class; reconstructions by the 30-dimensional autoencoder; reconstructions by 30-dimensional logistic PCA and standard PCA. The average squared errors for the last three rows are 3.00, 8.01, and 13.87. (C) Top to bottom: Random samples from the test data set; reconstructions by the 30-dimensional autoencoder; reconstructions by 30-dimensional PCA. The average squared errors are 126 and 135.



adjusting the weights and biases to lower the energy of that image and to raise the energy of similar, “confabulated” images that the network would prefer to the real data. Given a training image, the binary state h_j of each feature detector j is set to 1 with probability $\sigma(b_j + \sum_i v_i w_{ij})$, where $\sigma(x)$ is the logistic function $1/[1 + \exp(-x)]$, b_j is the bias of j , v_i is the state of pixel i , and w_{ij} is the weight between i and j . Once binary states have been chosen for the hidden units, a “confabulation” is produced by setting each v_i to 1 with probability $\sigma(b_i + \sum_j h_j w_{ij})$, where b_i is the bias of i . The states of

the hidden units are then updated once more so that they represent features of the confabulation. The change in a weight is given by

$$\Delta w_{ij} = \varepsilon (\langle v_i h_j \rangle_{\text{data}} - \langle v_i h_j \rangle_{\text{recon}}) \quad (2)$$

where ε is a learning rate, $\langle v_i h_j \rangle_{\text{data}}$ is the fraction of times that the pixel i and feature detector j are on together when the feature detectors are being driven by data, and $\langle v_i h_j \rangle_{\text{recon}}$ is the corresponding fraction for confabulations. A simplified version of the

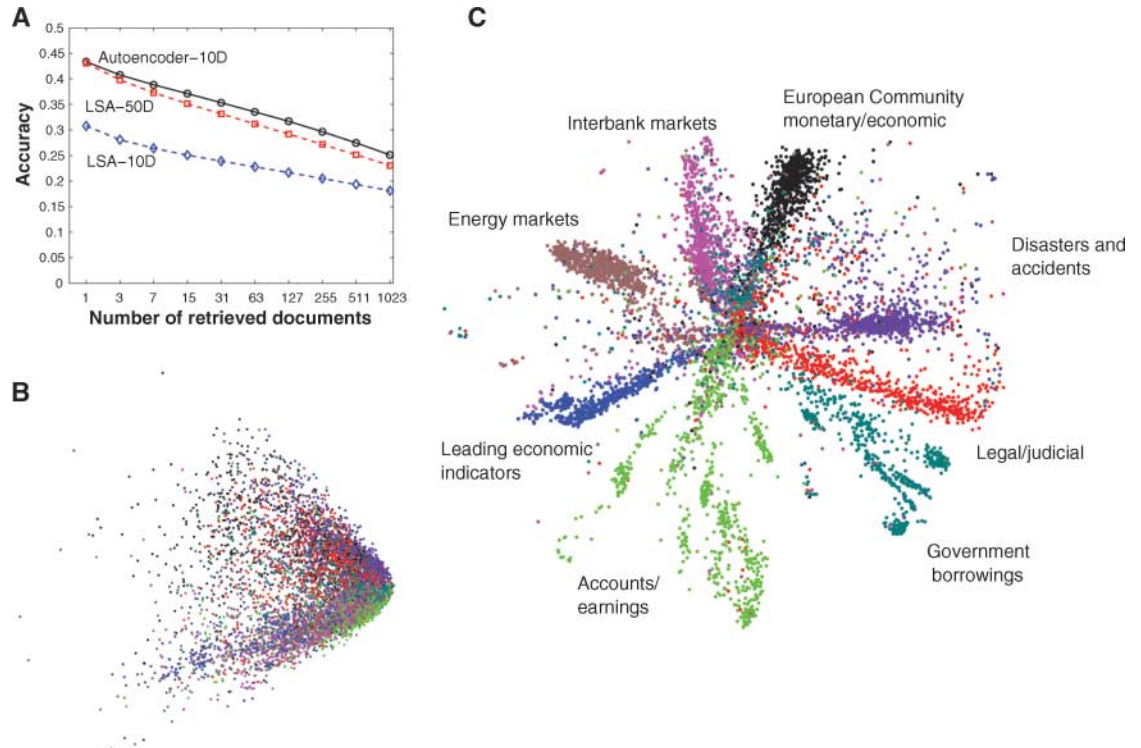
same learning rule is used for the biases. The learning works well even though it is not exactly following the gradient of the log probability of the training data (6).

A single layer of binary features is not the best way to model the structure in a set of images. After learning one layer of feature detectors, we can treat their activities—when they are being driven by the data—as data for learning a second layer of features. The first layer of feature detectors then become the visible units for learning the next RBM. This **layer-by-layer** learning can be repeated as many

Fig. 3. (A) The two-dimensional codes for 500 digits of each class produced by taking the first two principal components of all 60,000 training images. **(B)** The two-dimensional codes found by a 784-1000-500-250-2 autoencoder. For an alternative visualization, see (8).



Fig. 4. (A) The fraction of retrieved documents in the same class as the query when a query document from the test set is used to retrieve other test set documents, averaged over all 402,207 possible queries. **(B)** The codes produced by two-dimensional LSA. **(C)** The codes produced by a 2000-500-250-125-2 autoencoder.



times as desired. It can be shown that adding an extra layer always improves a lower bound on the log probability that the model assigns to the training data, provided the number of feature detectors per layer does not decrease and their weights are initialized correctly (9). This bound does not apply when the higher layers have fewer feature detectors, but the layer-by-layer learning algorithm is nonetheless a very effective way to pretrain the weights of a deep autoencoder. Each layer of features captures strong, **high-order correlations between the activities of units in the layer below**. For a wide variety of data sets, this is an efficient way to progressively reveal low-dimensional, nonlinear structure.

After pretraining multiple layers of feature detectors, the model is “unfolded” (Fig. 1) to produce encoder and decoder networks that initially use the same weights. The global fine-tuning stage then replaces stochastic activities by deterministic, real-valued probabilities and uses backpropagation through the whole autoencoder to fine-tune the weights for optimal reconstruction.

For continuous data, the hidden units of the first-level RBM remain binary, but the visible units are replaced by linear units with Gaussian noise (10). If this noise has unit variance, the stochastic update rule for the hidden units remains the same and the update rule for visible unit i is to sample from a Gaussian with unit variance and mean $b_i + \sum_j h_j w_{ji}$.

In all our experiments, the visible units of every RBM had real-valued activities, which were in the range [0, 1] for logistic units. While training higher level RBMs, the visible units were set to the activation probabilities of the hidden units in the previous RBM, but the hidden units of every RBM except the top one had stochastic binary values. The hidden units of the top RBM had stochastic real-valued states drawn from a unit variance Gaussian whose mean was determined by the input from that RBM’s logistic visible units. This allowed the low-dimensional codes to make good use of continuous variables and facilitated comparisons with PCA. Details of the pretraining and fine-tuning can be found in (8).

To demonstrate that our pretraining algorithm allows us to fine-tune deep networks efficiently, we trained a very deep autoencoder on a synthetic data set containing images of “curves” that were generated from three randomly chosen points in two dimensions (8). For this data set, the true intrinsic dimensionality is known, and the relationship between the pixel intensities and the six numbers used to generate them is highly nonlinear. The pixel intensities lie between 0 and 1 and are very non-Gaussian, so we used logistic output units in the autoencoder, and the fine-tuning stage of the learning minimized the **cross-entropy error** $[-\sum_i p_i \log \hat{p}_i - \sum_i (1 - p_i) \log(1 - \hat{p}_i)]$, where

p_i is the intensity of pixel i and \hat{p}_i is the intensity of its reconstruction.

The autoencoder consisted of an encoder with layers of size (28×28) -400-200-100-50-25-6 and a symmetric decoder. The six units in the code layer were linear and all the other units were logistic. The network was trained on 20,000 images and tested on 10,000 new images. The autoencoder discovered how to convert each 784-pixel image into six real numbers that allow almost perfect reconstruction (Fig. 2A). PCA gave much worse reconstructions. Without pretraining, the very deep autoencoder always reconstructs the average of the training data, even after prolonged fine-tuning (8). Shallower autoencoders with a single hidden layer between the data and the code can learn without pretraining, but pretraining greatly reduces their total training time (8). When the number of parameters is the same, deep autoencoders can produce lower reconstruction errors on test data than shallow ones, but this advantage disappears as the number of parameters increases (8).

Next, we used a 784-1000-500-250-30 autoencoder to extract codes for all the handwritten digits in the MNIST training set (11). The Matlab code that we used for the pretraining and fine-tuning is available in (8). Again, all units were logistic except for the 30 linear units in the code layer. After fine-tuning on all 60,000 training images, the autoencoder was tested on 10,000 new images and produced much better reconstructions than did PCA (Fig. 2B). A two-dimensional autoencoder produced a better visualization of the data than did the first two principal components (Fig. 3).

We also used a 625-2000-1000-500-30 autoencoder with linear input units to discover 30-dimensional codes for grayscale image patches that were derived from the Olivetti face data set (12). The autoencoder clearly outperformed PCA (Fig. 2C).

When trained on documents, autoencoders produce codes that allow fast retrieval. We represented each of 804,414 newswire stories (13) as a vector of document-specific probabilities of the 2000 commonest word stems, and we trained a 2000-500-250-125-10 autoencoder on half of the stories with the use of the multiclass cross-entropy error function $[-\sum_i p_i \log \hat{p}_i]$ for the fine-tuning. The 10 code units were linear and the remaining hidden units were logistic. When the cosine of the angle between two codes was used to measure similarity, the autoencoder clearly outperformed latent semantic analysis (LSA) (14), a well-known document retrieval method based on PCA (Fig. 4). Autoencoders (8) also outperform local linear embedding, a recent nonlinear dimensionality reduction algorithm (15).

Layer-by-layer pretraining can also be used for classification and regression. On a widely used version of the MNIST handwritten digit recogni-

tion task, the best reported error rates are 1.6% for randomly initialized backpropagation and 1.4% for support vector machines. After layer-by-layer pretraining in a 784-500-500-2000-10 network, backpropagation using steepest descent and a small learning rate achieves 1.2% (8). Pretraining helps generalization because it ensures that most of the information in the weights comes from modeling the images. The very limited information in the labels is used only to slightly adjust the weights found by pretraining.

It has been obvious since the 1980s that **backpropagation through deep autoencoders** would be very effective for nonlinear dimensionality reduction, provided that computers were **fast enough**, **data sets were big enough**, and the **initial weights** were close enough to a good solution. All three conditions are now satisfied. Unlike nonparametric methods (15, 16), autoencoders give mappings in both directions between the data and code spaces, and they can be applied to very large data sets because both the pretraining and the fine-tuning scale linearly in time and space with the number of training cases.

References and Notes

1. D. C. Plaut, G. E. Hinton, *Comput. Speech Lang.* **2**, 35 (1987).
2. D. DeMers, G. Cottrell, *Advances in Neural Information Processing Systems 5* (Morgan Kaufmann, San Mateo, CA, 1993), pp. 580–587.
3. R. Hecht-Nielsen, *Science* **269**, 1860 (1995).
4. N. Kambhathla, T. Leen, *Neural Comput.* **9**, 1493 (1997).
5. P. Smolensky, *Parallel Distributed Processing: Volume 1: Foundations*, D. E. Rumelhart, J. L. McClelland, Eds. (MIT Press, Cambridge, 1986), pp. 194–281.
6. G. E. Hinton, *Neural Comput.* **14**, 1711 (2002).
7. J. J. Hopfield, *Proc. Natl. Acad. Sci. U.S.A.* **79**, 2554 (1982).
8. See supporting material on Science Online.
9. G. E. Hinton, S. Osindero, Y. W. Teh, *Neural Comput.* **18**, 1527 (2006).
10. M. Welling, M. Rosen-Zvi, G. Hinton, *Advances in Neural Information Processing Systems 17* (MIT Press, Cambridge, MA, 2005), pp. 1481–1488.
11. The MNIST data set is available at <http://yann.lecun.com/exdb/mnist/index.html>.
12. The Olivetti face data set is available at www.cs.toronto.edu/~roweis/data.html.
13. The Reuter Corpus Volume 2 is available at <http://trec.nist.gov/data/reuters/reuters.html>.
14. S. C. Deerwester, S. T. Dumais, T. K. Landauer, G. W. Furnas, R. A. Harshman, *J. Am. Soc. Inf. Sci.* **41**, 391 (1990).
15. S. T. Roweis, L. K. Saul, *Science* **290**, 2323 (2000).
16. J. A. Tenenbaum, V. J. de Silva, J. C. Langford, *Science* **290**, 2319 (2000).
17. We thank D. Rumelhart, M. Welling, S. Osindero, and S. Roweis for helpful discussions, and the Natural Sciences and Engineering Research Council of Canada for funding. G.E.H. is a fellow of the Canadian Institute for Advanced Research.

Supporting Online Material

www.sciencemag.org/cgi/content/full/313/5786/504/DC1
Materials and Methods
Figs. S1 to S5
Matlab Code

20 March 2006; accepted 1 June 2006
10.1126/science.1127647